



**Stabilized open metal sites in bimetallic metal-organic  
framework catalysts for hydrogen production from alcohols**

Journal:	<i>Journal of Materials Chemistry A</i>
Manuscript ID	TA-ART-01-2021-000222.R1
Article Type:	Paper
Date Submitted by the Author:	26-Mar-2021
Complete List of Authors:	<p>Snider, Jonathan; Sandia National Laboratories California            Su, Ji; Lawrence Berkeley National Laboratory, Materials Sciences Division            Verma, Pragya; Lawrence Berkeley National Laboratory, Molecular Foundry            El Gabaly, Farid; Sandia National Laboratories California            Sugar, Joshua; Sandia National Laboratories California            Chen, Luning; Lawrence Berkeley National Laboratory, Materials Sciences Division            Chames, Jeffery; Sandia National Laboratories California            Talin, A.; Sandia National Laboratories California            Dun, Chaochao; Lawrence Berkeley National Laboratory, Molecular Foundry            Urban, Jeffrey; Lawrence Berkeley National Laboratory, Molecular Foundry            Stavila, Vitalie; Sandia National Laboratories California            Prendergast, David; Lawrence Berkeley National Laboratory, Molecular Foundry            Somorjai, Gabor; Lawrence Berkeley National Laboratory, Materials Sciences Division; University of California Berkeley, Department of Chemistry            Allendorf, Mark; Sandia National Laboratories California</p>

## ARTICLE

## Stabilized open metal sites in bimetallic metal-organic framework catalysts for hydrogen production from alcohols

Received 00th January 20xx,  
Accepted 00th January 20xx

DOI: 10.1039/x0xx00000x

Jonathan L. Snider,<sup>a</sup> Ji Su,<sup>b</sup> Pragya Verma,<sup>c</sup> Farid El Gabaly,<sup>a</sup> Joshua D. Sugar,<sup>a</sup> Luning Chen,<sup>b</sup> Jeffery M. Chames,<sup>a</sup> A. Alec Talin,<sup>a</sup> Chaochao Dun,<sup>c</sup> Jeffrey J. Urban,<sup>c</sup> Vitalie Stavila,<sup>a</sup> David Prendergast,<sup>c</sup> Gabor A. Somorjai,<sup>b,d</sup> and Mark D. Allendorf<sup>\*a</sup>

Liquid organic hydrogen carriers such as alcohols and polyols are a high-capacity means of transporting and reversibly storing hydrogen that demands effective catalysts to drive the (de)hydrogenation reactions under mild conditions. We employed a combined theory/experiment approach to develop MOF-74 catalysts for alcohol dehydrogenation and examine the performance of the open metal sites (OMS), which have properties analogous to the active sites in high-performance single-site catalysts and homogeneous catalysts. Methanol dehydrogenation was used as a model reaction system for assessing the performance of five monometallic M-MOF-74 variants (M = Co, Cu, Mg, Mn, Ni). Co-MOF-74 and Ni-MOF-74 give the highest H<sub>2</sub> productivity. However, Ni-MOF-74 is unstable under reaction conditions and forms metallic nickel particles. To improve catalyst activity and stability, bimetallic (Ni<sub>x</sub>Mg<sub>1-x</sub>)-MOF-74 catalysts were developed that stabilize the Ni OMS and promote the dehydrogenation reaction. An optimal composition exists at (Ni<sub>0.32</sub>Mg<sub>0.68</sub>)-MOF-74 that gives the greatest H<sub>2</sub> productivity, up to 203 mL g<sub>cat</sub><sup>-1</sup> min<sup>-1</sup> at 300 °C, and maintains 100% selectivity to CO and H<sub>2</sub> between 225-275 °C. The optimized catalyst is also active for the dehydrogenation of other alcohols. DFT calculations reveal that synergistic interactions between the open metal site and the organic linker lead to lower reaction barriers in the MOF catalysts compared to the open metal site alone. This work expands the suite of hydrogen-related reactions catalyzed by MOF-74 which includes recent work on hydroformulation and our earlier reports of aryl-ether hydrogenolysis. Moreover, it highlights the use of bimetallic frameworks as an effective strategy for stabilizing a high density of catalytically active open metal sites.

### Introduction

Hydrogen has long been regarded as a promising sustainable fuel and energy carrier; however, its direct utilization is a challenge because of the low volumetric energy density of hydrogen gas and high cost of storage and transportation.<sup>4, 5</sup> In contrast to other hydrogen storage approaches, such as compressed gas or solid-state storage in metal hydrides<sup>6</sup> and metal-organic frameworks (MOFs),<sup>7, 8</sup> liquid-organic hydrogen carriers (LOHCs) can provide high reversible capacities, chemical stability, low-cost transport, and would be compatible with existing infrastructure for fossil fuels as liquid energy vectors.<sup>9-12</sup> This concept involves storing hydrogen as hydrogen-rich liquid molecular carriers that are converted to H<sub>2</sub>(gas) for

stationary applications by breaking chemical bonds, typically in the presence of a catalyst.

Current research efforts focus on developing efficient carriers and advanced catalysts to increase reaction rates and provide a more stable hydrogen generation and storage process. To achieve a high hydrogen capacity, researchers have investigated a number of promising LOHCs, including several alcohol-based molecules: methanol (12.1 wt% H<sub>2</sub>),<sup>13-15</sup> ethylene glycol (6.5 wt% H<sub>2</sub>),<sup>16</sup> and other alcohols<sup>17</sup>. Although methanol is a high capacity hydrogen carrier, it requires the separation of CO to produce high purity hydrogen gas, making it less attractive for use with fuel cells where even minor CO contamination can lead to catalyst poisoning.<sup>18</sup> Polyols, such as ethylene glycol, could avoid these concerns by reacting to form pure gaseous hydrogen and a condensable hydrogen-lean byproduct.<sup>16</sup> Ultimately, the selection of LOHC will be dependent on the needs of the end use application; however, each will require a catalyst for the cycling reactions.

Supported transition metal catalysts have been developed for alcohol steam reforming, but poor hydrogen selectivity and deactivation remain challenging.<sup>19, 20</sup> Alternatively, acceptorless dehydrogenation simplifies the reaction chemistry by removing the need for an external oxidant.<sup>21</sup> However, the activity of the supported transition metal catalysts is significantly lower without water in the feed.<sup>22, 23</sup> High activity and selectivity can be achieved for acceptorless dehydrogenation through the use

<sup>a</sup> Sandia National Laboratories

7011 East Ave MS 9161, Livermore, CA, 94550, USA

<sup>b</sup> Materials Sciences Division, Lawrence Berkeley National Laboratory  
Building 66, One Cyclotron Road, Berkeley, CA 94720, USA

<sup>c</sup> Molecular Foundry, Lawrence Berkeley National Laboratory  
Building 67, One Cyclotron Road, Berkeley, CA, 94720, USA

<sup>d</sup> Department of Chemistry, University of California – Berkeley  
D56 Hildebrand Hall, Berkeley, CA, 94720, USA

\* Corresponding author, e-mail: mdallen@sandia.gov

† J. L. S. and J. S. contributed equally to this work.

Electronic Supplementary Information (ESI) available: Additional experimental methods, catalyst characterization, dehydrogenation results, methanol conversion, and DFT calculations. See DOI: 10.1039/x0xx00000x

of homogeneous metal complexes.<sup>24</sup> These catalysts have disadvantages as well, including high cost, poor stability, and difficult reusability. To access the full hydrogen capacity under mild reaction conditions, researchers are seeking catalysts with lower costs while being highly active, selective, and stable.

Coordinatively unsaturated metal sites, like the catalytically active centers present in many metal complexes, have been shown to trigger different reaction pathways and improve performance over traditional metallic catalysts. For example, the introduction of phosphate ligands to silica-supported Ni<sup>2+</sup> improves selectivity toward propane dehydrogenation by stabilizing the single-site Ni<sup>2+</sup> and preventing the formation of methane-selective metallic Ni<sup>0</sup>.<sup>25</sup> Similarly, homogeneous catalysts based on Ni<sup>2+</sup> complexes are found to be highly selective for the dehydrogenation of alcohols.<sup>26, 27</sup>

Toward the goal of creating an improved catalyst, single metal site catalysts are attracting great interest due to their atom-utilization efficiency, unique structure, and improved performance.<sup>28-30</sup> However, because traditional heterogeneous catalyst supports (e.g. metal oxides) can exhibit facets and anchoring sites with vastly different surface energies, it is difficult to achieve structural homogeneity or a high density of active sites.<sup>31-33</sup> Moreover, the lack of an ensemble of active atoms adjacent to the metal atom in most single metal site catalysts prevents surface reactions that involve large molecules or multiple adsorbates.<sup>34, 35</sup> Finding an ideal support to permit a high loading of structurally homogeneous and highly active single metal sites is one of the present challenges in heterogeneous catalysis.

Metal-Organic Frameworks (MOFs) have emerged as a tunable platform to create coordinatively unsaturated single metal sites, or open metal sites (OMS), within a uniform porous support. MOFs feature a well-defined structure, chemically and structurally uniform active sites, and rational design via judicious choice of molecular building blocks.<sup>36-41</sup> Single sites within MOFs can be engineered as immobilized elements, on the node or linker, or as encapsulated species.<sup>37</sup> Creating reactive OMS in MOFs is among the most attractive strategies as these can present similar local environments to those of high-performance homogeneous catalysts.<sup>42, 43</sup> The long-range order of MOFs eliminates the structural variability present in traditional solid-phase supports and offers precise control of chemical functionality to modulate the reaction selectivity and delineate structure-property relationships. Furthermore, chemical functionalities in the local environment around the OMS, such as oxygen-containing carboxylate groups, provides active atoms adjacent to the single metal atom that promote the adsorption, activation, reaction, and desorption of molecules. Catalysts based on the MOF-74 structure have been demonstrated for a variety of reactions, including C–H oxidation,<sup>44-48</sup> NO<sub>x</sub> reduction,<sup>49</sup> hydroformulation,<sup>50</sup> water dissociation,<sup>51</sup> CO<sub>2</sub> conversion,<sup>52, 53</sup> and ether hydrogenolysis.<sup>54, 55</sup> This demonstrates that the divalent OMS in MOF-74 has great potential to combine the best of homogeneous and heterogeneous catalysis by providing a tunable and specific catalyst with an extended and uniform array of single metal sites.

Here, we demonstrate that OMS in the isostructural series M-MOF-74 (M<sub>2</sub>(dobdc), where M = Co, Cu, Mg, Mn, Ni and dobdc = 2,5-dioxido-1,4-benzenedicarboxylate) catalyze the dehydrogenation of alcohols. The MOF-74 topology has the highest-known volumetric density of OMS, and the nickel version, which contains square pyramidal Ni<sup>2+</sup> OMS, is an unexplored coordination environment for nickel-based dehydrogenation catalysts. A key issue, however, is that Ni-MOF-74 has poor thermal and structural stability.<sup>56, 57</sup> To improve stability, bimetallic MOF-74 structures have previously been found to stabilize Mg-MOF-74 against hydrolysis.<sup>58</sup> We hypothesize that a partial substitution of Ni into the nodes of Mg-MOF-74 will give rise to catalytically active Ni<sup>2+</sup> OMS while also maintaining structural stability, thereby maximizing activity and selectivity for alcohol dehydrogenation.

## Methods

**(Ni<sub>x</sub>Mg<sub>1-x</sub>)-MOF-74 synthesis:** M-MOF-74 (M<sub>2</sub>(dobdc) where M = Ni, Mg, or Ni<sub>x</sub>Mg<sub>1-x</sub> and (dobdc) = 2,5-dioxido-1,4-benzenedicarboxylate) was synthesized using a solvothermal reaction of metal salts with 2,5-dihydroxyterephthalic acid. This procedure is slightly modified from one reported previously.<sup>54</sup> In a 250 mL glass bottle, 160 mL N,N-dimethylformamide (DMF), 8 mL ethanol, and 8 mL deionized water were mixed. To this, 0.41 g (2.1 mmol) of 2,5-dihydroxyterephthalic acid was dissolved via sonication. Next, 6.2 mmol of a mixture of anhydrous magnesium(II) chloride and anhydrous nickel(II) chloride was added (about a 50% excess relative to dobdc). The metal chlorides were added in the synthesis ratios prescribed in Table S4. In all cases, the bottles were then tightly capped, and the mixtures were sonicated until well dissolved. In some cases, the solutions remained turbid, but turned clear upon mild heating. The bottles were heated in an oven at 120 °C. After 16 hours, the samples were removed from the oven and cooled. A solid material was recovered via centrifugation, washed with 50 mL DMF, and soaked for several hours. This washing procedure was repeated once more with DMF and three additional times with methanol. The solid was then collected by centrifugation and dried under a nitrogen flow. After drying, the MOF was activated under dynamic vacuum at 170 °C for 16 hours and transferred, air-free, to a nitrogen glovebox for storage. Synthetic methods used for the monometallic MOFs, similar to those above, are detailed in the Supporting Information, Section S1.

**Catalytic Testing:** The catalytic activity of all MOF-74 catalysts toward hydrogen production from methanol was evaluated in a continuous flow reactor. Methanol (CH<sub>3</sub>OH, 99.9%), ethanol (C<sub>2</sub>H<sub>5</sub>OH, 99.8%), n-propanol (n-C<sub>3</sub>H<sub>7</sub>OH, 99.7%), isopropanol (CH<sub>3</sub>CH(OH)CH<sub>3</sub>, 99.5%), butyl alcohol (C<sub>4</sub>H<sub>9</sub>OH, 99.5%), benzyl alcohol (C<sub>6</sub>H<sub>5</sub>CH<sub>2</sub>OH, 99.8%), and ethylene glycol (CH<sub>2</sub>(OH)CH<sub>2</sub>(OH), 99.8%) were purchased from Sigma-Aldrich. All reagents were used without further purification.

In a typical catalytic experiment, 100 mg of catalyst was first mixed with 500 mg of glass beads (50-70 mesh particle size). The

mixture was packed in a fixed-bed flow reactor with quartz wool plugs. Then methanol liquid was pumped into the heating chamber with a feeding rate of 0.1 ml/min. In the heating chamber, methanol vapor mixes with carrier gas N<sub>2</sub> (35 ml/min) before entering the reactor tube. Pressure was maintained at 1 atm. The temperature of the bed was monitored by a K-type thermocouple, and the furnace was controlled by a PID 679 controller. The products were analyzed on-stream by a HP 5890 gas chromatograph (Hayesep D column and Hayesep Q column, N<sub>2</sub> carrier gas) equipped with a thermal conductivity detector and a flame ionization detector. Any liquid products were also collected and measured by NMR (AV-700). Metrics for catalytic performance were calculated as shown in the Supporting Information, Section S1.

After catalysis, the catalyst bed was removed from the reactor tube. To remove contamination by quartz wool and glass, the samples were cleaned prior to further characterization. Samples were first sieved with a 140 mesh sieve to remove the grains of sand, yielding a small amount of usable powder. When characterization required additional powder, the sand grains were washed with methanol to give a colored liquid which was dried under N<sub>2</sub> to yield additional spent catalyst. Since BET measurements would be especially sensitive to low surface area contaminants, such as the quartz wool and sand, the methanol-washed material was used for N<sub>2</sub> isotherms.

Sample collection was generally performed with air exposure, except for the catalysts collected after reaction at 250°C. For these samples, the reactor tube was sealed under nitrogen and opened in a nitrogen-containing glovebox. Samples were mounted for TEM and XPS within the glovebox and transferred air-free to the characterization instruments.

**X-ray photoelectron spectroscopy (XPS):** XPS data was collected at Sandia National Laboratories at ambient temperature, using samples adhered to carbon tape or dropcast onto Au foil from a suspension in methanol. The samples were mounted into a steel stage that was then affixed to a custom-designed clean transfer system that allows air-sensitive samples to be sealed within either an inert atmosphere or vacuum, and which can be attached to the XPS UHV chamber for insertion without exposure to air or moisture. The X-ray source was an Al K-alpha anode (PE = 1486.7 eV). Analysis of all XPS spectra was performed using the CasaXPS peak-fitting software, using Shirley backgrounds and appropriate constraints for each element. FWHM were held constant across the peaks within a given spectral region, with multiple peaks being included to fit the complex satellite peak regions. Spectra were calibrated to the adventitious C 1s peak (284.8 eV), which allows for internal referencing of the binding energies.

**X-ray diffraction (XRD):** XRD patterns were collected on a Rigaku SmartLab using Cu K $\alpha$  radiation generated at 40 kV and 44 mA. Measurements were collected in air on powder samples that were spread onto glass slides. Scans were conducted between 4 and 80 degrees, with a step size of 0.05 degrees, and a scan rate of about 5 degrees per minute.

**Nitrogen isotherms:** Isotherms and Brunauer, Emmett and Teller (BET) surface area measurements were carried out at 77 K using either a Micromeritics ASAP 2020 porosimeter or a Quantachrome Autosorb iQ porosimeter with liquid N<sub>2</sub> cooling. Prior to each measurement, samples were degassed at 170 °C under vacuum for 16 hours.

**Transmission electron microscopy (TEM):** TEM images were collected on a ThermoFisher Titan Themis Z operated at 300 kV. The Themis Z is equipped with a probe Cs-corrector and a large-angle four quadrant SuperX EDS detector (~0.7 sr). Energy dispersive spectrum (EDS) images were collected with 10-20  $\mu$ sec pixel times, a probe current of approximately 150 – 200 pA, and the application of automatic drift correction. Samples were prepared in air by sonicating the sample materials in methanol and drop casting the solution onto Cu lacey carbon grids.

**Scanning electron microscopy (SEM):** SEM images were collected with a JEOL JSM7600F Thermal Field Emission Electron Microscope. EDS analysis was performed with an Oxford Instruments X-MaxN 80 Detector combined with Oxford's Aztec software. Microscope conditions for both imaging and EDS spectrum capture were: accelerating voltage of 15 kV, probe current setting of 10, and a working distance of 8 mm. Samples were prepared for SEM by pressing the powders into indium foil, to avoid carbon contamination from other adhesive techniques. Spectra were collected at positions and magnifications to yield sufficient powder thickness to block signal from the underlying indium.

**Theoretical approach:** Density functional theory (DFT) calculations were performed on the unit cell of M-MOF-74 with periodic boundary conditions as implemented in *Vienna Ab Initio Simulation Package (VASP)*.<sup>59, 60</sup> For the periodic model, a unit cell consisting of 54 atoms (3 formula units of M<sub>2</sub>(dobdc)), of which six are metal atoms, is used. The metal atoms are arranged in two chains (Figure S9) with three in each chain. The DFT methods used are the generalized gradient approximation, PBE,<sup>61</sup> the van der Waals density functional, rev-vdW-DF2,<sup>62</sup> and the +U corrected rev-vdW-DF2+U method, where on-site Hubbard *U* correction<sup>63, 64</sup> is applied to the open-shell 3*d* *e*-s of the transition metals, Mn, Co, Ni, and Cu of M-MOF-74. The choice of +U is based on published recommendations.<sup>65</sup> For all the periodic DFT calculations performed in this work, we optimized the nuclear positions, cell shape, and unit cell volume using plane-wave basis sets and projector-augmented-wave potentials<sup>66, 67</sup> provided with the VASP package. These calculations were performed using a *k*-point mesh of 4x2x2 was used to sample the Brillouin zone, a cutoff energy of 600 eV, a self-consistent field energy convergence criterion of 10<sup>-6</sup> eV, and a force convergence criterion of -10<sup>-3</sup> eV/Å.

To probe the mechanism of conversion of methanol to carbon monoxide catalyzed by M-MOF-74, we used an 88-atom cluster model<sup>68</sup> with three metal atoms and six organic ligands (Figure S9), carved from the aforementioned periodic models.

These were then optimized using either the rev-vdW-DF2 method (for Mg-MOF-74 and Zn-MOF-74) or the rev-vdW-DF2+U (for Mn-MOF-74, Co-MOF-74, Ni-MOF-74, and Cu-MOF-74) method. Only the central metal atom and the five oxygen atoms of the cluster were optimized, with the remaining atoms frozen. The cluster is terminated using H atoms and a high-spin ground state is used with the three metal ions of the cluster ferromagnetically coupled. For each species involved in the reaction – reactants, intermediates, transition structures, and products – we performed a partial optimization of the cluster, whereby the central metal atom, its first coordination sphere, and any adsorbate interacting with the central metal atom were optimized. These calculations were performed with the PBE exchange-correlation functional and the def2-SVP or the def2-TZVP basis set<sup>69</sup> using the *Gaussian 16* suite of quantum mechanical programs.<sup>70</sup>

## Results and Discussion

### Monometallic M-MOF-74 catalysts

To evaluate the methanol dehydrogenation performance of M-MOF-74, a series of five catalysts were prepared (M = Co, Cu, Mg, Mn, and Ni) by solvothermal synthesis. Most of the catalyst series was found to feature the high surface areas typical of the MOF-74 structure (Figure S1). Cu-MOF-74, Co-MOF-74, Mg-MOF-74, and Ni-MOF-74 had BET surface areas ranging from 1050–1510 m<sup>2</sup> g<sup>-1</sup>, whereas Mn-MOF-74 had a lower surface area of 490 m<sup>2</sup> g<sup>-1</sup>. X-ray diffraction (XRD) confirmed the MOF-74 structure in all five samples (Figure 1a). Small peak shifts are observed from the simulated Mg-MOF-74 reference, most notably in Mn-MOF-74, consistent with the expanded metal-metal distances predicted by DFT (Table S1) and reported for previously synthesized MOF-74 frameworks.<sup>71</sup> Given the constant topology five porous MOF-74 structures synthesized, the identity of the OMS is expected to drive differences in catalytic performance.

The catalyst performance towards methanol dehydrogenation was evaluated in a flow reactor at 1 atm and up to 300 °C. The results, shown in Figure 1b–c, reveal that Mg-MOF-74 and Mn-MOF-74 are both inactive for the reaction under these conditions. Cu-MOF-74 exhibited low H<sub>2</sub> productivity ( $\leq 42$  mL H<sub>2</sub> g<sub>cat</sub><sup>-1</sup> min<sup>-1</sup>) and high dimethyl ether (DME) selectivity ( $\geq 10.9$  %). Co-MOF-74 and Ni-MOF-74 are significantly more active than the other MOFs, exhibiting the highest H<sub>2</sub> productivity and CO selectivity of the series. The H<sub>2</sub> productivity of Co-MOF-74 increases from near zero at 200 °C to 117.1 mL H<sub>2</sub> g<sub>cat</sub><sup>-1</sup> min<sup>-1</sup> at 300 °C with 100 % CO selectivity. Ni-MOF-74 produces even more H<sub>2</sub>, as much as 158.1 mL H<sub>2</sub> g<sub>cat</sub><sup>-1</sup> min<sup>-1</sup> at 300 °C. However, this coincides with a loss in CO selectivity, with 5.3 % methane selectivity observed at 300 °C. Comparing Co-MOF-74 and Ni-MOF-74, the performance is similar until about 250 °C; at this temperature Ni-MOF-74 begins to catalyze methane production. In contrast, Co-MOF-74 is nearly 100% selective towards syngas (CO + H<sub>2</sub>). Due to the well-documented propensity of metallic nickel for

methanation<sup>72, 73</sup> and Ni-MOF-74's poor thermal stability<sup>56, 58</sup> (Ni nanoparticle formation observed as low as 200 °C under vacuum<sup>74</sup>), this finding suggests that Ni-MOF-74 is degrading to form nickel nanoparticles.

To test this hypothesis, samples of Co-MOF-74 and Ni-MOF-74 were characterized before and after performing catalysis at 250 °C for one hour. Under these conditions, the Co-MOF-74 catalyst was stable. Prior to reaction, transmission electron microscopy (TEM) images reveal a rod-like morphology with homogeneous composition throughout (Figure 2a), consistent with previous reports on Co-MOF-74.<sup>75, 76</sup> A small number of clusters with high oxygen content are also observed. Similar morphology and composition distributions are observed after catalysis testing (Figure 2b). X-ray photoelectron spectroscopy (XPS) indicates that the Co<sup>2+</sup> nodes in the MOF (780.7 eV) are unchanged by the reaction (Figure 2c). Furthermore, the X-ray diffraction (XRD) patterns obtained before and after reaction indicate that the crystal structure is also intact (Figure 2d). Together, the characterization identifies Co-MOF-74 as a robust material for methanol dehydrogenation at 250 °C.

In contrast, Ni-MOF-74 is unstable under the catalysis conditions, consistent with prior results on Ni-MOF-74 stability.<sup>74</sup> This is first apparent visually via a darkening of the initial yellow powder to become brown and eventually black (Figure S2). The initial flake-like morphology of the MOF (Figure 3a) is dotted with small nanoparticles of nickel after performing methanol dehydrogenation, as shown in Figure 3b by the appearance of bright spots in the dark field TEM and green clusters in the EDS mapping. These particles were found to agglomerate into large clusters of nickel. Particle formation is also evidenced by XPS data showing that a shoulder forms on the Ni<sup>2+</sup> peak of the MOF (856.3eV) after catalysis that is assigned to metallic Ni<sup>0</sup> at 852.8 eV (Figure 3c). Comparing the areas of the Ni<sup>2+</sup> and Ni<sup>0</sup> features, ~18% of the nickel is reduced after one hour on stream at 250 °C. Post-catalysis XRD reveals that a broad Ni(111) peak at 44.6° has also formed (Figure 3d), consistent with the small nanoparticles observed in TEM. A featureless band is also observed between 10 - 40°, consistent with the formation of amorphous carbon species upon framework degradation. The presence of amorphous carbon is further supported by significant broadening of the Raman bands of the tested sample between 1200–1700 cm<sup>-1</sup> (Figure S3). TEM and PXRD data obtained from a sample after catalysis at 300 °C reveals that the decomposition is even more severe at higher temperatures, forming large nickel agglomerates and sharp Ni(111) peaks (Figure S4). As will be discussed later, the observed framework degradation correlates with a significant deactivation of the catalytic activity after six hours on stream (Figure S5). Consequently, a stabilization strategy must be developed if the highly active Ni OMS of Ni-MOF-74 is to be used for methanol dehydrogenation.

### Bimetallic (Ni<sub>x</sub>Mg<sub>1-x</sub>)-MOF-74 catalysts

Building upon these results, we sought to stabilize the Ni OMS and determine whether its already high activity could be improved. Since the stability of the MOF-74 framework under

the reaction conditions varies with the metal used, we hypothesized that a partial substitution of the unstable Ni OMS into a more stable framework would inhibit the precipitation of metallic nickel nanoparticles. Mixed-metal MOFs have been previously investigated for a variety of applications, including catalysis, in which they prove to be a highly tunable approach to improve performance.<sup>58, 77-81</sup> For this study, Ni-Mg was selected as the target system due to several key advantages. First, Mg-MOF-74 features much greater thermal and chemical stability than any of the other versions of MOF-74, up to 400 °C.<sup>82, 83</sup> Second, activity arising from the Ni OMS can be readily assessed as our results (Fig. 1b) demonstrate that Mg-MOF-74 is catalytically inactive. Finally, the propensity of metallic Ni for methanation makes methane selectivity a useful diagnostic for particle formation and MOF stability.

A series of five bimetallic (Ni<sub>x</sub>Mg<sub>1-x</sub>)-MOF-74 catalysts were synthesized using a modified one-pot solvothermal synthesis method whereby the ratio of Ni to Mg precursors was varied from 0.01 to 0.6. A 50% excess of the metal precursor relative to the organic linker was used to ensure full conversion of the linker molecule. This altered the elemental composition obtained in the final product as the Ni OMS was found to be preferentially incorporated into the bimetallic framework (Table S2). For example, when a Ni:Mg ratio of 0.25 was used for solvothermal synthesis, the final product had a Ni:Mg ratio of 0.47, as determined by scanning electron microscopy and energy dispersive spectroscopy (SEM-EDS) and checked with inductively coupled plasma-optical emission spectroscopy (ICP-OES). This is consistent with preferential incorporation into the MOF structure of the excess NiCl<sub>2</sub> in solution. This phenomenon can be understood by the higher stability of Mg<sup>2+</sup> in solution compared to Ni<sup>2+</sup>. The Mg<sup>2+</sup> ion has a standard heat of formation of -462 kJ mol<sup>-1</sup> in aqueous media vs. -64 kJ mol<sup>-1</sup> for Ni<sup>2+</sup>.<sup>84</sup> A preferential uptake of metals has been observed previously in multimetallic MOFs made via one-pot syntheses.<sup>58, 85</sup> The final metal ratios of the catalyst series, as listed in Table S2, were determined by SEM-EDS and are used in naming the catalyst samples henceforth. A discussion and comparison of the SEM-EDS and ICP-OES results can be found in the Supporting Information (Section S2).

The MOF-74 structure was confirmed by PXRD for the catalyst series (Figure 4a). No peaks corresponding to metallic nickel (e.g. Ni(111) at 44.6°) were observed. Minor contractions in the MOF-74 structure were observed in some samples as the nickel fraction increased, particularly for (Ni<sub>0.76</sub>Mg<sub>0.24</sub>)-MOF-74. This is consistent with the subtle decrease in metal-metal distance predicted by DFT for Ni-MOF-74 relative to Mg-MOF-74. However, because the "as synthesized" PXRD was collected on air-exposed samples, this effect is masked by expansion of the frameworks upon adsorption of guest molecules, such as moisture from the air or residual methanol (Table S1). N<sub>2</sub> isotherms were also collected for the bimetallic catalyst series and again confirm that high BET surface areas were achieved, ranging from 910-1510 m<sup>2</sup> g<sup>-1</sup> (Figure S6). Together, these results establish that our synthetic method produces the MOF-74 topology across the composition series.

The results of methanol dehydrogenation experiments across the (Ni<sub>x</sub>Mg<sub>1-x</sub>)-MOF-74 catalyst series are presented in Figure 4b-d and show that, between 200-250 °C, the highest H<sub>2</sub> productivity is found when using MOFs with Ni fractions of x = 0.32 or higher. At higher temperatures, H<sub>2</sub> productivity increases up to x = 0.32, at which point productivity decreases with increasing Ni fraction (Figure 4b). Excellent CO selectivity, greater than 99.5%, is observed at all temperatures for Ni fractions up to x = 0.32. As the Ni fraction is increased above x = 0.32, DME selectivity and methane selectivity both increase with increasing nickel content. DME selectivity decreases with increasing temperature, whereas methane selectivity increases with increasing temperature (Figure 4c). The increasing methane selectivity of the Ni-rich compositions is indicative of nickel particle formation in those catalysts. As a result, an optimal composition exists at (Ni<sub>0.32</sub>Mg<sub>0.68</sub>)-MOF-74 that gives the greatest H<sub>2</sub> productivity, up to 203 mL g<sub>cat</sub><sup>-1</sup> min<sup>-1</sup> at 300 °C, while also maintaining 100% selectivity to syngas between 225-275 °C. By the previously established correlation between Ni particle formation and methane selectivity, we infer that this MOF composition yields the greatest number of active Ni OMS and maintains high stability within the Mg framework.

Post-catalysis characterization of the (Ni<sub>0.32</sub>Mg<sub>0.68</sub>)-MOF-74 catalyst confirms that the bimetallic framework stabilizes the Ni OMS. Characterization was performed on the bimetallic catalyst before and after one hour of testing at 250 °C, the temperature at which Ni-MOF-74 was previously found to have significant particle formation. As was seen with Ni-MOF-74, the "as synthesized" (Ni<sub>0.32</sub>Mg<sub>0.68</sub>)-MOF-74 takes the form of flakes with uniform elemental distribution (Figure 5a). After catalysis at 250 °C, the morphology of (Ni<sub>0.32</sub>Mg<sub>0.68</sub>)-MOF-74 is unchanged, with no evidence for particle formation observed via TEM (Figure 5b). Additional confirmation is provided by XPS analysis (Figure 5c). Spectra in the Ni 2p region show no change to the (Ni<sub>0.32</sub>Mg<sub>0.68</sub>)-MOF-74 catalyst after testing at 250 °C. The spectra can be fit solely with the MOF-74 Ni<sup>2+</sup> peak at 855.8 eV and its satellite peaks. The Mg 1s region is also unchanged at all temperatures tested (Figure S7). Raman spectroscopy of the sample after one hour of catalysis is consistent with that of the starting material, suggesting that the framework has not degraded (Figure S3). Finally, MOF-74 remains the sole crystalline phase observed by XRD after testing at 250 °C (Figure 5d). At the higher reaction temperature of 300 °C, the bimetallic catalyst degrades, forming Ni nanoparticles (Figure S8a-d). This coincides with the methane selectivity of (Ni<sub>0.32</sub>Mg<sub>0.68</sub>)-MOF-74 increasing to 0.2%, reinforcing the utility of methane selectivity as a diagnostic. Despite the appearance of metallic Ni, the bimetallic framework remains stable enough to maintain a high BET surface area of 850 m<sup>2</sup> g<sup>-1</sup> even after testing at 300 °C (Figure S8e). Overall, post-reaction characterization reveals that embedding the Ni OMS within a stable Mg-MOF-74 framework increases the stability of the reactive Ni OMS, creating an improved catalyst for methanol dehydrogenation with high productivity and up to 100% CO selectivity.

A continuous stability test at 250 °C, the temperature at which selectivity is maximized across the series, clearly reveals the increased stability achieved by the bimetallic catalyst

(Figure 4d). Comparing the most active catalyst ((Ni<sub>0.32</sub>Mg<sub>0.68</sub>)-MOF-74) with monometallic Ni-MOF-74, we find that the stability of the bimetallic catalyst is significantly higher than that of the monometallic version. The bimetallic catalyst loses 29% of its initial activity over 24 hours, whereas Ni-MOF-74 loses 42% over just six hours. Very high selectivity is also maintained in the bimetallic case with CO selectivity remaining at or above 99.6% over 24 hours. This is in stark contrast to Ni-MOF-74, for which the CO selectivity drops to 94.2% after only six hours due to methane selectivity rising to 5.8%. The gradual degradation of the bimetallic catalyst correlates with the loss of the Ni<sup>2+</sup> OMS. After one hour, when performance is still at its maximum, TEM-EDS, XPS, XRD, and Raman characterizations do not reveal any evidence for framework degradation (Figure 5). After 24 hours on stream, the performance has degraded and characterization by XPS and Raman reveals the formation of Ni<sup>0</sup> and amorphous carbon respectively (Figure S9 and Figure S3).

As our measurements show that the Mg OMS is inactive for methanol dehydrogenation, the Ni OMS can be identified as the active site for the bimetallic catalyst series. To examine the intrinsic activity of this site, the hydrogen productivity was normalized to the nickel content of each catalyst as determined by SEM-EDS. Even when normalized to Ni, the (Ni<sub>0.32</sub>Mg<sub>0.68</sub>)-MOF-74 catalyst still provides the greatest H<sub>2</sub> productivity of the series, 1501 mL H<sub>2</sub> g<sub>Ni</sub><sup>-1</sup> min<sup>-1</sup> (Figure 6). On the basis of methanol consumed, the turnover frequency (TOF) of the Ni OMS in (Ni<sub>0.32</sub>Mg<sub>0.68</sub>)-MOF-74 is calculated to be 31.4 hr<sup>-1</sup> at 250 °C and 105 hr<sup>-1</sup> at 300 °C, competitive with many transition metal catalysts (Table S3). Two assumptions were made in computing this value: (1) the Ni OMS is the active site of the reaction and (2) all reactive nickel is in the form of an OMS. If the amount of accessible reactive Ni is less than this, as, for example, the result of the observed degradation over time or if the reaction occurs primarily at the surface of the MOF particles, the computed TOF values would be a lower limit of true TOF of the OMS.

The comparison in Figure 6 with Raney Ni, which we tested under equivalent conditions, demonstrates that the optimal MOF is much more selective than this commercial catalyst. Raney Ni is pyrophoric upon drying, so care was taken to handle the material under a N<sub>2</sub> atmosphere while loading and unloading the reactor. The Ni-normalized activity of (Ni<sub>0.32</sub>Mg<sub>0.68</sub>)-MOF-74 is comparable to Raney Ni at high temperatures. As shown in Table S3, the TOF of Raney Ni is estimated to be 36.5–41 hr<sup>-1</sup> at 250 °C compared to 31.4 hr<sup>-1</sup> for the bimetallic MOF. However, the OMS of the MOF catalyst has a significant selectivity advantage when compared to the metallic sites in Raney Ni. (Ni<sub>0.32</sub>Mg<sub>0.68</sub>)-MOF-74 has a methane selectivity of 0% at 250 °C and 0.2% at 300 °C. In contrast, Raney Ni has 15.3% and 23% methane selectivity, respectively, at those conditions (Figure S10).

The (Ni<sub>0.32</sub>Mg<sub>0.68</sub>)-MOF-74 catalyst is also active for the dehydrogenation of other hydrogen carriers. We evaluated (Ni<sub>0.32</sub>Mg<sub>0.68</sub>)-MOF-74 for hydrogen production from a variety of alcohol-based carriers: ethylene glycol, ethanol, 1-propanol, and 2-propanol. As shown in Figure 7, the catalyst produces hydrogen at high rates from all of these molecules. This

versatility creates the potential for situations in which the selection of carrier varies, for example depending on cost, seasonal availability, or materials compatibility.

#### DFT investigation of MOF-74 catalysts

To understand the experimental trends and gain insight into how the OMS participates in the reaction, we performed a computational study for a series of M-MOF-74 structures (M = Co, Cu, Mg, Mn, Ni, Zn). Density functional theory (DFT) calculations were applied to two models, as shown in Figure S11: a periodic model with 54 atoms (three formula units of M<sub>2</sub>(dobdc)) and a cluster model with 88-atoms constrained at its periphery to reproduce the local structure within the periodic model.<sup>68</sup> The cluster model allows calculations to be run on a system that is small enough to perform accurate DFT calculations while still being large enough to capture the behavior of the full catalyst structure (see Table S4 for a comparison between cluster and periodic models).

We first computed the binding energy of several adsorbates for each M-MOF-74 structure using the periodic model at 0 K. The results indicate that all metals readily absorb methanol, with exoergic adsorption energies between -11.6 and -21.7 kcal mol<sup>-1</sup> (Table S5). This behavior is consistent with prior observations of methanol adsorption in MOF-74 frameworks.<sup>51, 75</sup> In all cases, the lowest energy configuration for methanol was found to be binding via the oxygen atom. The cluster model was also used to predict the energetics of CO binding at the OMS, which is also predicted to be exoergic, regardless of whether the CO is bound via carbon or oxygen (Table S6). In all cases, binding via the carbon atom yielded the lowest energy configuration. Notably, the binding energies to Co and Ni, -18.8 kcal mol<sup>-1</sup> and -15.8 kcal mol<sup>-1</sup> respectively, are about ~10 kcal/mol stronger than the other metals.

The cluster model was then used to investigate the reaction energetics and determine whether the linker plays a role in the catalysis. Two reactions were considered: dehydrogenation of methanol to formaldehyde (Reaction 1) and the subsequent dehydrogenation of formaldehyde to carbon monoxide (Reaction 2).<sup>86</sup>



For the species involved in each reaction – reactants, intermediates, transition structures, and products – a partial optimization of the cluster was performed in which the positions of the adsorbate, the active metal site, and the five linker oxygen atoms in the first coordination sphere of the OMS were optimized. Frequency calculations were performed in the optimized degrees of freedom to include temperature effects and the enthalpies were calculated by adding the zero-point vibrational energy and thermal contributions at 298.15 K and 1 atm pressure. The intermediate structures were characterized by the presence of only real frequencies and the transition structures were characterized by the presence of one imaginary frequency. This analysis provided the transition state for specific steps along the dehydrogenation pathway. Given the large multiplicity of possible landing points for reactants and

products in the MOF framework around each metal site, we limited our analysis to selected key transition states, shown in the free energy diagram in Figure 8 for Ni-MOF-74. Transition states for other M-MOF-74 structures can be found in the Supporting Information (Figures S12 and S13).

When the reaction proceeds via the OMS alone (i.e. without adsorbate interaction with the linker oxygen atom), highly unfavorable reaction energies (Table 1) are observed, with barrier heights ( $\Delta G^\ddagger$ )  $>70$  kcal mol<sup>-1</sup> for both reaction steps across all the metals surveyed. These energies are comparable to the uncatalyzed (gas-phase) reaction. However, if the adsorbate is permitted to interact with both the OMS and the neighboring organic linker via its oxygen atom, the transition state orientations shown in Figures 8 are obtained. The resulting barrier heights are dramatically reduced to a few kcal mol<sup>-1</sup> for Reaction 1 and 48 – 64 kcal mol<sup>-1</sup> for Reaction 2. The high barriers for Reaction 2 are consistent with the elevated temperatures required in the catalysis tests. Additional information, including reaction enthalpies (Table S7) and visualizations of the reduced barrier heights (Figure S14), can be found in the Supporting Information.

Looking closer at the individual reaction steps, the linker-assisted dehydrogenation of methanol to formaldehyde is found to be exergonic and exhibits barriers less than 12 kcal mol<sup>-1</sup> for all metals surveyed (Table 1). Ni and Mg have the lowest barriers at 1.9 kcal mol<sup>-1</sup> and 1.3 kcal mol<sup>-1</sup>, respectively. In contrast, the subsequent dehydrogenation to CO is endergonic. The computed barriers for Reaction 2 are similar in magnitude across the metal series, with Cu and Mg giving the highest barriers at 63.1 kcal mol<sup>-1</sup> and 61.4 kcal mol<sup>-1</sup> respectively and Ni and Co having the lowest barriers at 47.3 kcal mol<sup>-1</sup> and 48.3 kcal mol<sup>-1</sup>, respectively. Based on these results we expect that Reaction 2 will be rate-limiting, requiring high temperatures to achieve a significant turnover. The experimental reaction results weakly correlate with the activation barriers shown in Table 1. The catalysts with the highest barriers (Cu-MOF-74, Mg-MOF-74) have little to no activity and those with the lowest barriers (Co-MOF-74, Ni-MOF-74) being the most active of the series. The hydrogen productivity also correlates with the calculated CO binding energy, with the strongest binding Ni-MOF-74 and Co-MOF-74 catalysts giving the greatest hydrogen productivity of the series.

The free energy diagram in Figure 8 provides a mechanistic picture of the reaction using Ni-MOF-74 as a representative example. Before Reaction 1, there is first adsorption of methanol onto the metal site via its oxygen atom, followed by transfer of a hydrogen atom to a neighboring linker oxygen atom (TS0). The methoxy adsorbate on the OMS is bent over toward the linker oxygen (TS1), giving a geometry that facilitates the release of H<sub>2</sub> by a heterolytic recombination (proton from the linker and hydride from the methyl) to produce formaldehyde (Reaction 1). The formaldehyde is adsorbed to the metal site via its oxygen atom and undergoes rotation (TS<sub>rot</sub>), leading to a structure in which the hydrogen atom interacts with the metal site. This rotation, with a barrier of 7.1 kcal mol<sup>-1</sup> is not rate-limiting. Finally, the oxygen atom of the linker is again able to assist by interacting with a

formaldehyde hydrogen (TS2), facilitating the release of carbon monoxide and the recombination of the two hydrogen atoms at the OMS to form the final unit of H<sub>2</sub> (Reaction 2). This is consistent with prior work showing that linker functionalities can play an active role in catalysis within MOFs, such as controlling product selectivity<sup>87</sup> or enantioselectivity.<sup>88, 89</sup>

## Conclusions

In this report we describe MOF-based catalysts developed for hydrogen production from alcohol-based hydrogen carriers using a combined experimental and theoretical approach. Five monometallic MOF-74 catalysts were evaluated for methanol dehydrogenation. Co-MOF-74 and Ni-MOF-74 were found to be the most active at 300 °C (117.1 and 158.1 mL H<sub>2</sub> g<sub>cat</sub><sup>-1</sup> min<sup>-1</sup> respectively). For Ni-MOF-74, however, decreasing activity and increasing methane selectivity were observed over time due to framework degradation and formation of metallic nickel particles. To improve performance and stabilize the Ni OMS, bimetallic frameworks were synthesized with partial substitution of Ni OMS into the inactive but stable Mg-MOF-74 framework. Bimetallic (Ni<sub>x</sub>Mg<sub>1-x</sub>)-MOF-74 catalysts demonstrated improved activity, selectivity and stability compared to Ni-MOF-74. An optimal composition was found at (Ni<sub>0.32</sub>Mg<sub>0.68</sub>)-MOF-74, with up to 203 mL H<sub>2</sub> g<sub>cat</sub><sup>-1</sup> min<sup>-1</sup> at 300 °C and 100% selectivity to syngas between 225-275 °C. TEM, XPS, XRD, and Raman characterization confirm that the (Ni<sub>0.32</sub>Mg<sub>0.68</sub>)-MOF-74 catalyst improves the stability of the Ni OMS. The bimetallic catalyst is also found to be broadly active for alcohol dehydrogenation and compatible with a number of hydrogen carriers.

The Ni-normalized activity of the bimetallic catalyst series was maximized at (Ni<sub>0.32</sub>Mg<sub>0.68</sub>)-MOF-74. At high temperatures, the Ni-normalized activity decreased with more Ni-rich compositions, consistent with the increased methane selectivity and framework instability observed in those samples. Conversely, the intrinsic activity increased from  $x=0.01$  to  $x=0.32$  indicating that composition tuning has promotional effects beyond simply stabilizing the framework; highlighting the tunability of MOF catalysts. However, even though activity was maximized at the (Ni<sub>0.32</sub>Mg<sub>0.68</sub>) composition, gradual degradation was still observed in the catalyst with high temperatures and extended time on stream. While the stability of the bimetallic catalyst is a marked improvement over the Ni-MOF-74 catalyst and demonstrates the effectiveness of this strategy, additional stabilization is still required. Future work is needed to understand the tuneability of these bimetallic frameworks and improve their stability.

The TOF for methanol dehydrogenation at the Ni OMS in (Ni<sub>0.32</sub>Mg<sub>0.68</sub>)-MOF-74 was estimated to be 32 hr<sup>-1</sup> at 250 °C and 105 hr<sup>-1</sup> at 300 °C. This value assumes all of the nickel is accessible to the reaction. Consequently, the computed TOF should be considered a lower limit. In future work we plan to use the tunable pore diameter of the structurally analogous IRMOF-74(n) series to determine whether mass transport limitations within the pore network are limiting the reaction kinetics.

Our DFT calculations for monometallic M-MOF-74 catalysts allow us to propose a reaction mechanism in which interactions between reacting species coordinated to the Ni OMS and the adjacent oxygen atom of the organic linker significantly reduce the reaction barriers. When using this linker-assisted mechanism, Ni-MOF-74 was found to have the lowest barrier for the rate-limiting step of the reaction (the dehydrogenation of formaldehyde). Given the large number of potential landing points for reaction species in the MOF, however, we do not consider this mechanism definitive. The lack of detectable formaldehyde in the product stream and the observed correlation between strong CO binding and high H<sub>2</sub> productivity also could be consistent with alternative methanol dehydrogenation pathways. Future studies will examine the full range of pathways for methanol dehydrogenation, including mechanisms for reabsorption and poisoning, which may give an improved alignment with the reaction trends observed among the monometallic catalyst series.

Overall, this work demonstrates that MOF-74 is an effective platform for developing single-site alcohol dehydrogenation catalysts. The activity, selectivity, and stability of monometallic MOF-74 can be enhanced by engineering a bimetallic framework. This provides another illustration of the tremendous tuneability of MOF catalysts. It also motivates future studies to fully understand the observed performance enhancements, further improve the stability of the catalysts, and extend this strategy to other OMS catalysts such as the Co-MOF-74 reported here.

## Author Contributions

J.L.S. conducted synthesis, characterization, and analysis. J.S. and L.C. conducted catalytic testing. P.V. performed DFT calculations. F.E.G. performed XPS characterization. J.D.S. performed TEM characterization. J.M.C. performed SEM characterization. C.D. performed ICP-OES analysis. A.A.T. performed Raman characterization. J.L.S., J.S., V.S., and M.D.A. discussed and planned the project. D.P., G.A.S., and M.D.A. supervised the project. J.L.S. wrote the manuscript including significant contributions from J.S., P.V., and V.S. All authors discussed the results and reviewed the final manuscript.

## Conflicts of interest

There are no conflicts to declare.

## Acknowledgements

The authors gratefully acknowledge support from the Hydrogen Materials-Advanced Research Consortium (HyMARC), established as part of the Energy Materials Network under the U.S. Department of Energy, Office of Energy Efficiency and Renewable Energy, Hydrogen and Fuel Cell Technologies Office, under Contract Number DE-AC04-94AL85000. Sandia National Laboratories is a multimission laboratory managed and operated by National Technology and Engineering Solutions of Sandia, LLC, a wholly owned subsidiary of Honeywell

International, Inc., for the U.S. Department of Energy's National Nuclear Security Administration under contract DE-NA-0003525.

We thank High Performance Computing Services at Lawrence Berkeley National Laboratory and Minnesota Supercomputing Institute at the University of Minnesota for computational resources. Work at the Molecular Foundry was supported by the Office of Science, Office of Basic Energy Sciences, of the U.S. Department of Energy under Contract No. DE-AC02-05CH11231.

The authors gratefully acknowledge both Dr. Matthijs van Spronsen at Lawrence Berkeley National Laboratory and Dr. Michael E. Foster for their time and fruitful discussions of the project.

The views and opinions of the authors expressed herein do not necessarily state or reflect those of the United States Government or any agency thereof. Neither the United States Government nor any agency thereof, nor any of their employees, makes any warranty, expressed or implied, or assumes any legal liability or responsibility for the accuracy, completeness, or usefulness of any information, apparatus, product, or process disclosed, or represents that its use would not infringe privately owned rights.

## References

1. P. D. C. Dietzel, R. Blom and H. Fjellvåg, *Eur. J. Inorg. Chem.*, 2008, **2008**, 3624-3632.
2. P. D. C. Dietzel, Y. Morita, R. Blom and H. Fjellvåg, *Angew. Chem. Int. Ed.*, 2005, **44**, 6354-6358.
3. P. D. C. Dietzel, B. Panella, M. Hirscher, R. Blom and H. Fjellvåg, *Chem. Commun.*, 2006, 959-961.
4. F. Dawood, M. Anda and G. M. Shafiullah, *Int. J. Hydrog. Energy*, 2020, **45**, 3847-3869.
5. S. Koochi-Fayegh and M. A. Rosen, *J. Energy Storage*, 2020, **27**, 101047.
6. A. Schneemann, J. L. White, S. Kang, S. Jeong, L. F. Wan, E. S. Cho, T. W. Heo, D. Prendergast, J. J. Urban, B. C. Wood, M. D. Allendorf and V. Stavila, *Chem. Rev.*, 2018, **118**, 10775-10839.
7. M. D. Allendorf, Z. Hulvey, T. Gennett, A. Ahmed, T. Autrey, J. Camp, E. Seon Cho, H. Furukawa, M. Haranczyk, M. Head-Gordon, S. Jeong, A. Karkamkar, D.-J. Liu, J. R. Long, K. R. Meihaus, I. H. Nayyar, R. Nazarov, D. J. Siegel, V. Stavila, J. J. Urban, S. P. Veccham and B. C. Wood, *Energy Environ. Sci.*, 2018, **11**, 2784-2812.
8. M. P. Suh, H. J. Park, T. K. Prasad and D. W. Lim, *Chem. Rev.*, 2012, **112**, 782-835.
9. M. Markiewicz, Y. Q. Zhang, A. Bösmann, N. Brückner, J. Thöming, P. Wasserscheid and S. Stolte, *Energy Environ. Sci.*, 2015, **8**, 1035-1045.
10. M. Niermann, A. Beckendorff, M. Kaltschmitt and K. Bonhoff, *Int. J. Hydrog. Energy*, 2019, **44**, 6631-6654.
11. P. Preuster, C. Papp and P. Wasserscheid, *Acc. Chem. Res.*, 2017, **50**, 74-85.
12. P. M. Modisha, C. N. M. Ouma, R. Garidzirai, P. Wasserscheid and D. Bessarabov, *Energy Fuels*, 2019, **33**, 2778-2796.
13. Y. Xie, P. Hu, Y. Ben-David and D. Milstein, *Angew. Chem. Int. Ed.*, 2019, **58**, 5105-5109.
14. T.-W. Liao, A. Yadav, P. Ferrari, Y. Niu, X.-K. Wei, J. Vernieres, K.-J. Hu, M. Heggen, R. E. Dunin-Borkowski, R. E.

- Palmer, K. Laasonen, D. Grandjean, E. Janssens and P. Lievens, *Chem. Mater.*, 2019, **31**, 10040-10048.
15. L. N. Chen, K. P. Hou, Y. S. Liu, Z. Y. Qi, Q. Zheng, Y. H. Lu, J. Y. Chen, J. L. Chen, C. W. Pao, S. B. Wang, Y. B. Li, S. H. Xie, F. D. Liu, D. Prendergast, L. E. Klebanoff, V. Stavila, M. D. Allendorf, J. Guo, L. S. Zheng, J. Su and G. A. Somorjai, *J. Am. Chem. Soc.*, 2019, **141**, 17995-17999.
16. Y.-Q. Zou, N. von Wolff, A. Anaby, Y. Xie and D. Milstein, *Nat. Catal.*, 2019, **2**, 415-422.
17. P. J. Bonitatibus, Jr., S. Chakraborty, M. D. Doherty, O. Siclován, W. D. Jones and G. L. Soloveichik, *PNAS*, 2015, **112**, 1687-1692.
18. X. Cheng, Z. Shi, N. Glass, L. Zhang, J. Zhang, D. Song, Z.-S. Liu, H. Wang and J. Shen, *J. Power Sources*, 2007, **165**, 739-756.
19. S. D. Davidson, H. Zhang, J. Sun and Y. Wang, *Dalton Trans.*, 2014, **43**, 11782-11802.
20. A. Kubacka, M. Fernández-García and A. Martínez-Arias, *Appl. Catal. A*, 2016, **518**, 2-17.
21. K.-i. Shimizu, K. Kon, M. Seto, K. Shimura, H. Yamazaki and J. N. Kondo, *Green Chem.*, 2013, **15**, 418-424.
22. Y. Choi and H. G. Stenger, *Appl. Catal. B*, 2002, **38**, 259-269.
23. N. Takezawa and N. Iwasa, *Catal. Today*, 1997, **36**, 45-56.
24. M. Trincado, D. Banerjee and H. Grützmacher, *Energy Environ. Sci.*, 2014, **7**, 2464-2503.
25. G. Zhang, C. Yang and J. T. Miller, *ChemCatChem*, 2018, **10**, 961-964.
26. S. Chakraborty, P. E. Piszal, W. W. Brennessel and W. D. Jones, *Organometallics*, 2015, **34**, 5203-5206.
27. Z. Dai, Q. Luo, H. Jiang, Q. Luo, H. Li, J. Zhang and T. Peng, *Catal. Sci. Technol.*, 2017, **7**, 2506-2511.
28. L. Liu and A. Corma, *Chem. Rev.*, 2018, **118**, 4981-5079.
29. A. Wang, J. Li and T. Zhang, *Nat. Rev. Chem.*, 2018, **2**, 65-81.
30. S. Ji, Y. Chen, X. Wang, Z. Zhang, D. Wang and Y. Li, *Chem. Rev.*, 2020, **120**, 11900-11955.
31. H. Ha, S. Yoon, K. An and H. Y. Kim, *ACS Catal.*, 2018, **8**, 11491-11501.
32. J. Höcker, J.-O. Krispeneit, T. Schmidt, J. Falta and J. I. Flege, *Nanoscale*, 2017, **9**, 9352-9358.
33. M. Nolan and G. W. Watson, *J. Phys. Chem. B*, 2006, **110**, 16600-16606.
34. H. Jeong, G. Lee, B.-S. Kim, J. Bae, J. W. Han and H. Lee, *J. Am. Chem. Soc.*, 2018, **140**, 9558-9565.
35. Y. J. Hwang, Y. Kwon, Y. Kim, H. Sohn, S. W. Nam, J. Kim, T. Autrey, C. W. Yoon, Y. S. Jo and H. Jeong, *Acs Sustain Chem Eng*, 2020, **8**, 9846-9856.
36. L. Jiao and H.-L. Jiang, *Chem*, 2019, **5**, 786-804.
37. M. C. Wasson, C. T. Buru, Z. Chen, T. Islamoglu and O. K. Farha, *Appl. Catal. A*, 2019, **586**, 117214.
38. S. M. J. Rogge, A. Bavykina, J. Hajek, H. Garcia, A. I. Olivios-Suarez, A. Sepúlveda-Escribano, A. Vimont, G. Clet, P. Bazin, F. Kapteijn, M. Daturi, E. V. Ramos-Fernandez, F. X. Llabrés i Xamena, V. Van Speybroeck and J. Gascon, *Chem. Soc. Rev.*, 2017, **46**, 3134-3184.
39. V. Pascanu, G. González Miera, A. K. Inge and B. Martín-Matute, *J. Am. Chem. Soc.*, 2019, **141**, 7223-7234.
40. D. Yang and B. C. Gates, *ACS Catal.*, 2019, **9**, 1779-1798.
41. C. Wang, B. An and W. Lin, *ACS Catal.*, 2019, **9**, 130-146.
42. J. N. Hall and P. Bollini, *React. Chem. Eng.*, 2019, **4**, 207-222.
43. Ü. Kökçam-Demir, A. Goldman, L. Esrafilı, M. Gharib, A. Morsali, O. Weingart and C. Janiak, *Chem. Soc. Rev.*, 2020, **49**, 2751-2798.
44. D. J. Xiao, J. Oktawiec, P. J. Milner and J. R. Long, *J. Am. Chem. Soc.*, 2016, **138**, 14371-14379.
45. P. Verma, K. D. Vogiatzis, N. Planas, J. Borycz, D. J. Xiao, J. R. Long, L. Gagliardi and D. G. Truhlar, *J. Am. Chem. Soc.*, 2015, **137**, 5770-5781.
46. E. D. Bloch, W. L. Queen, S. Chavan, P. S. Wheatley, J. M. Zadrozny, R. Morris, C. M. Brown, C. Lamberti, S. Bordiga and J. R. Long, *J. Am. Chem. Soc.*, 2015, **137**, 3466-3469.
47. J. Borycz, J. Paier, P. Verma, L. E. Darago, D. J. Xiao, D. G. Truhlar, J. R. Long and L. Gagliardi, *Inorg. Chem.*, 2016, **55**, 4924-4934.
48. D. J. Xiao, E. D. Bloch, J. A. Mason, W. L. Queen, M. R. Hudson, N. Planas, J. Borycz, A. L. Dzubak, P. Verma, K. Lee, F. Bonino, V. Crocellà, J. Yano, S. Bordiga, D. G. Truhlar, L. Gagliardi, C. M. Brown and J. R. Long, *Nat. Chem.*, 2014, **6**, 590-595.
49. H. Jiang, Q. Wang, H. Wang, Y. Chen and M. Zhang, *ACS Appl. Mater. Interfaces*, 2016, **8**, 26817-26826.
50. G. Bauer, D. Ongari, D. Tiana, P. Gaumann, T. Rohrbach, G. Pareras, M. Tarik, B. Smit and M. Ranocchiari, *Nat. Commun.*, 2020, **11**, 1059.
51. E. M. A. Fuentes-Fernandez, S. Jensen, K. Tan, S. Zuluaga, H. Wang, J. Li, T. Thonhauser and Y. J. Chabal, *Appl Sci*, 2018, **8**, 270.
52. D.-A. Yang, H.-Y. Cho, J. Kim, S.-T. Yang and W.-S. Ahn, *Energy Environ. Sci.*, 2012, **5**, 6465-6473.
53. I. Choi, Y. E. Jung, S. J. Yoo, J. Y. Kim, H.-J. Kim, C. Y. Lee and J. H. Jang, *J. Electrochem. Sci. Technol.*, 2017, **8**, 61-68.
54. V. Stavila, R. Parthasarathi, R. W. Davis, F. El Gabaly, K. L. Sale, B. A. Simmons, S. Singh and M. D. Allendorf, *ACS Catal.*, 2015, **6**, 55-59.
55. V. Stavila, M. E. Foster, J. W. Brown, R. W. Davis, J. Edgington, A. I. Benin, R. A. Zarkesh, R. Parthasarathi, D. W. Hoyt, E. D. Walter, A. Andersen, N. M. Washton, A. S. Lipton and M. D. Allendorf, *Chem. Sci.*, 2019, **10**, 9880-9892.
56. M. Mukoyoshi, H. Kobayashi, K. Kusada, M. Hayashi, T. Yamada, M. Maesato, J. M. Taylor, Y. Kubota, K. Kato, M. Takata, T. Yamamoto, S. Matsumura and H. Kitagawa, *Chem. Commun.*, 2015, **51**, 12463-12466.
57. S. Zuluaga, E. M. A. Fuentes-Fernandez, K. Tan, F. Xu, J. Li, Y. J. Chabal and T. Thonhauser, *J. Mater. Chem. A*, 2016, **4**, 5176-5183.
58. Y. Jiao, C. R. Morelock, N. C. Burtch, W. P. Mounfield, J. T. Hungerford and K. S. Walton, *Ind. Eng. Chem. Res.*, 2015, **54**, 12408-12414.
59. G. Kresse and J. Furthmüller, *Comput. Mater. Sci.*, 1996, **6**, 15-50.
60. G. Kresse and J. Furthmüller, *Phys. Rev. B*, 1996, **54**, 11169-11186.
61. J. P. Perdew, K. Burke and M. Ernzerhof, *Phys. Rev. Lett.*, 1996, **77**, 3865-3868.
62. I. Hamada, *Phys. Rev. B*, 2014, **89**, 121103.
63. A. I. Liechtenstein, V. I. Anisimov and J. Zaanen, *Phys. Rev. B*, 1995, **52**, R5467-R5470.
64. S. L. Dudarev, G. A. Botton, S. Y. Savrasov, C. J. Humphreys and A. P. Sutton, *Phys. Rev. B*, 1998, **57**, 1505-1509.
65. L. Wang, T. Maxisch and G. Ceder, *Phys. Rev. B*, 2006, **73**, 195107.
66. P. E. Blöchl, *Phys. Rev. B*, 1994, **50**, 17953-17979.

67. G. Kresse and D. Joubert, *Phys. Rev. B*, 1999, **59**, 1758-1775.
68. P. Verma, X. Xu and D. G. Truhlar, *J. Phys. Chem. C*, 2013, **117**, 12648-12660.
69. F. Weigend and R. Ahlrichs, *Phys. Chem. Chem. Phys.*, 2005, **7**, 3297-3305.
70. M. J. Frisch, G. W. Trucks, H. B. Schlegel, G. E. Scuseria, M. A. Robb, J. R. Cheeseman, G. Scalmani, V. Barone, G. A. Petersson, H. Nakatsuji, X. Li, M. Caricato, A. V. Marenich, J. Bloino, B. G. Janesko, R. Gomperts, B. Mennucci, H. P. Hratchian, J. V. Ortiz, A. F. Izmaylov, J. L. Sonnenberg, Williams, F. Ding, F. Lipparini, F. Egidi, J. Goings, B. Peng, A. Petrone, T. Henderson, D. Ranasinghe, V. G. Zakrzewski, J. Gao, N. Rega, G. Zheng, W. Liang, M. Hada, M. Ehara, K. Toyota, R. Fukuda, J. Hasegawa, M. Ishida, T. Nakajima, Y. Honda, O. Kitao, H. Nakai, T. Vreven, K. Throssell, J. A. Montgomery Jr., J. E. Peralta, F. Ogliaro, M. J. Bearpark, J. J. Heyd, E. N. Brothers, K. N. Kudin, V. N. Staroverov, T. A. Keith, R. Kobayashi, J. Normand, K. Raghavachari, A. P. Rendell, J. C. Burant, S. S. Iyengar, J. Tomasi, M. Cossi, J. M. Millam, M. Klene, C. Adamo, R. Cammi, J. W. Ochterski, R. L. Martin, K. Morokuma, O. Farkas, J. B. Foresman and D. J. Fox, *Journal*, 2016.
71. W. Zhou, H. Wu and T. Yildirim, *J. Am. Chem. Soc.*, 2008, **130**, 15268-15269.
72. M. Liu, S. Zhao, X. Xiao, M. Chen, C. Sun, Z. Yao, Z. Hu and L. Chen, *Nano Energy*, 2019, **61**, 540-549.
73. M. Matsukata, T. Hayashi, M. Nishiyama, E. Kikuchi and Y. Morita, *Sekiyu Gakkaishi*, 1987, **30**, 265.
74. T. C. Wang, J. L. White, B. Bie, H. Deng, J. Edgington, J. D. Sugar, V. Stavila and M. D. Allendorf, *ChemPhysChem*, 2019, **20**, 1305-1310.
75. I. Strauss, A. Mundstock, D. Hinrichs, R. Himstedt, A. Knebel, C. Reinhardt, D. Dorfs and J. Caro, *Angew. Chem. Int. Ed.*, 2018, **57**, 7434-7439.
76. J. Chen, X. Mu, M. Du and Y. Lou, *Inorg. Chem. Commun.*, 2017, **84**, 241-245.
77. J. A. Villajos, G. Orcajo, C. Martos, J. Á. Botas, J. Villacañas and G. Calleja, *Int. J. Hydrog. Energy*, 2015, **40**, 5346-5352.
78. M. Y. Masoomi, A. Morsali, A. Dhakshinamoorthy and H. Garcia, *Angew. Chem. Int. Ed.*, 2019, **58**, 15188-15205.
79. S. Abednatanzi, P. Gohari Derakhshandeh, H. Depauw, F.-X. Coudert, H. Vrielinck, P. Van Der Voort and K. Leus, *Chem. Soc. Rev.*, 2019, **48**, 2535-2565.
80. D. Sun, F. Sun, X. Deng and Z. Li, *Inorg. Chem.*, 2015, **54**, 8639-8643.
81. K. Yuan, T. Song, D. Wang, Y. Zou, J. Li, X. Zhang, Z. Tang and W. Hu, *Nanoscale*, 2018, **10**, 1591-1597.
82. S. R. Caskey, A. G. Wong-Foy and A. J. Matzger, *J. Am. Chem. Soc.*, 2008, **130**, 10870-10871.
83. V. Stavila, R. K. Bhakta, T. M. Alam, E. H. Majzoub and M. D. Allendorf, *ACS Nano*, 2012, **6**, 9807-9817.
84. Masterton, Slowinski and Stanitski, *Chemical principles*, CBS College Publishing, New York, 5th edn., 1983.
85. L. J. Wang, H. Deng, H. Furukawa, F. Gandara, K. E. Cordova, D. Peri and O. M. Yaghi, *Inorg. Chem.*, 2014, **53**, 5881-5883.
86. E. Jones and G. G. Fowlie, *J. Appl. Chem.*, 1953, **3**, 206-213.
87. G. Bauer, D. Ongari, X. Xu, D. Tian, B. Smit and M. Ranocchiari, *J. Am. Chem. Soc.*, 2017, **139**, 18166-18169.
88. C.-D. Wu, A. Hu, L. Zhang and W. Lin, *J. Am. Chem. Soc.*, 2005, **127**, 8940-8941.
89. M. Zheng, Y. Liu, C. Wang, S. Liu and W. Lin, *Chem. Sci.*, 2012, **3**, 2623-2627.

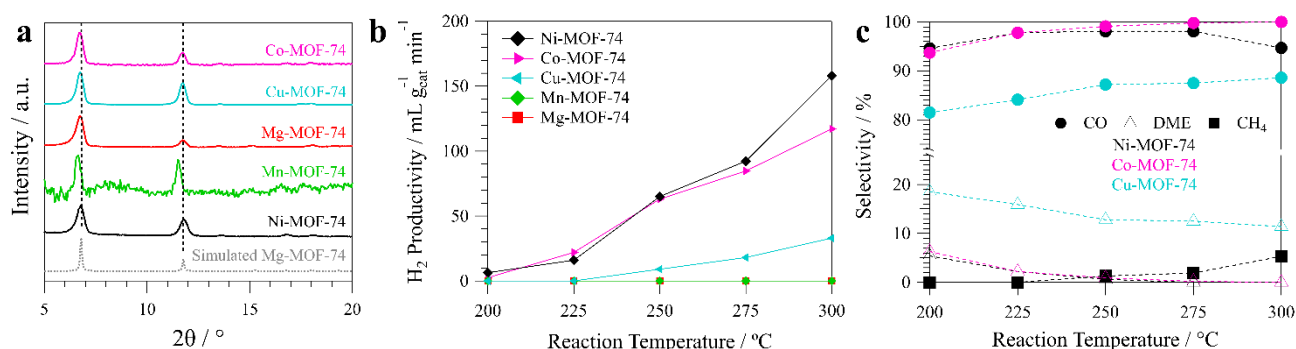


**Figure 1.** (a) Normalized XRD patterns of the 'as synthesized' M-MOF-74 catalyst series, compared against a simulated Mg-MOF-74 reference (CSD-VOGTIV).<sup>1</sup> Catalytic performance of the synthesized M-MOF-74 catalysts towards methanol dehydrogenation: (b) hydrogen productivity normalized to the total mass of catalyst and (c) product selectivity towards CO (solid circles), DME (open triangles) and CH<sub>4</sub> (solid squares). Reaction conditions: 0.1 mL min<sup>-1</sup> methanol, 35 sccm N<sub>2</sub>, 100 mg catalyst, 1 atm.

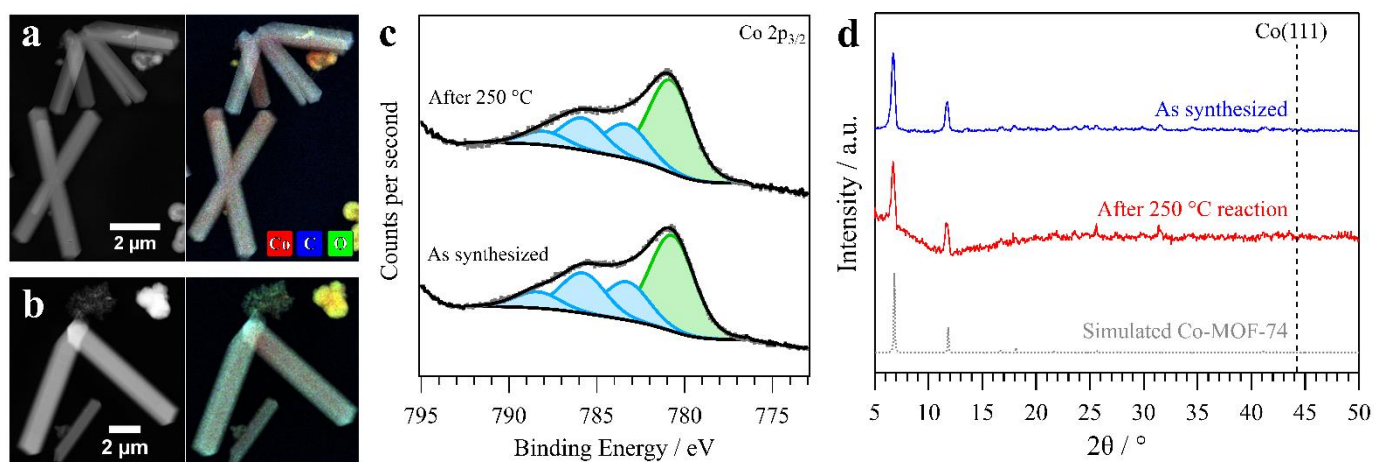


**Figure 2.** Characterization of Co-MOF-74 before and after performing methanol dehydrogenation for 1 hour at 250 °C and 1 atm. Dark field TEM images and TEM-EDS maps of the catalyst (a) before testing and (b) after testing, showing cobalt (red), carbon (blue), and oxygen (green). (c) Normalized Co 2p<sub>3/2</sub> XPS spectra of the catalyst before and after testing. Experimental data (grey points) fit with a Co<sup>2+</sup> peak (green) and several satellite peaks (blue) to create the envelope shown (black line). (d) Normalized XRD patterns of the catalyst before and after testing, compared to a simulated Co-MOF-74 reference (CSD-SATNOR).<sup>2</sup>

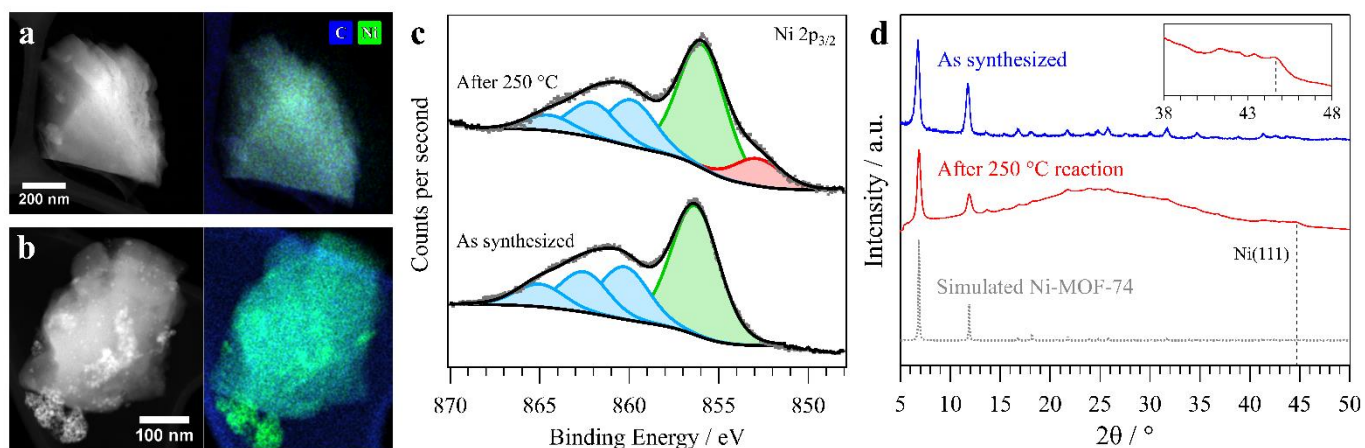


**Figure 3.** Characterization of Ni-MOF-74 before and after performing methanol dehydrogenation for 1 hour at 250 °C and 1 atm. Dark field TEM images and TEM-EDS maps of the catalyst (a) before testing and (b) after testing, showing carbon (blue) and nickel (green). (c) Normalized Ni 2p<sub>3/2</sub> XPS spectra of the catalyst before and after testing. Experimental data (grey points) fit with a Ni<sup>0</sup> peak (red), Ni<sup>2+</sup> peak (green), and several satellite peaks (blue) to create the envelope shown (black line). (d) Normalized XRD patterns of the catalyst before and after testing, compared to a simulated Ni-MOF-74 reference (CSD-LECQEQ).<sup>3</sup> Inset plot showing the Ni(111) peak observed in the sample after reaction at 250 °C.

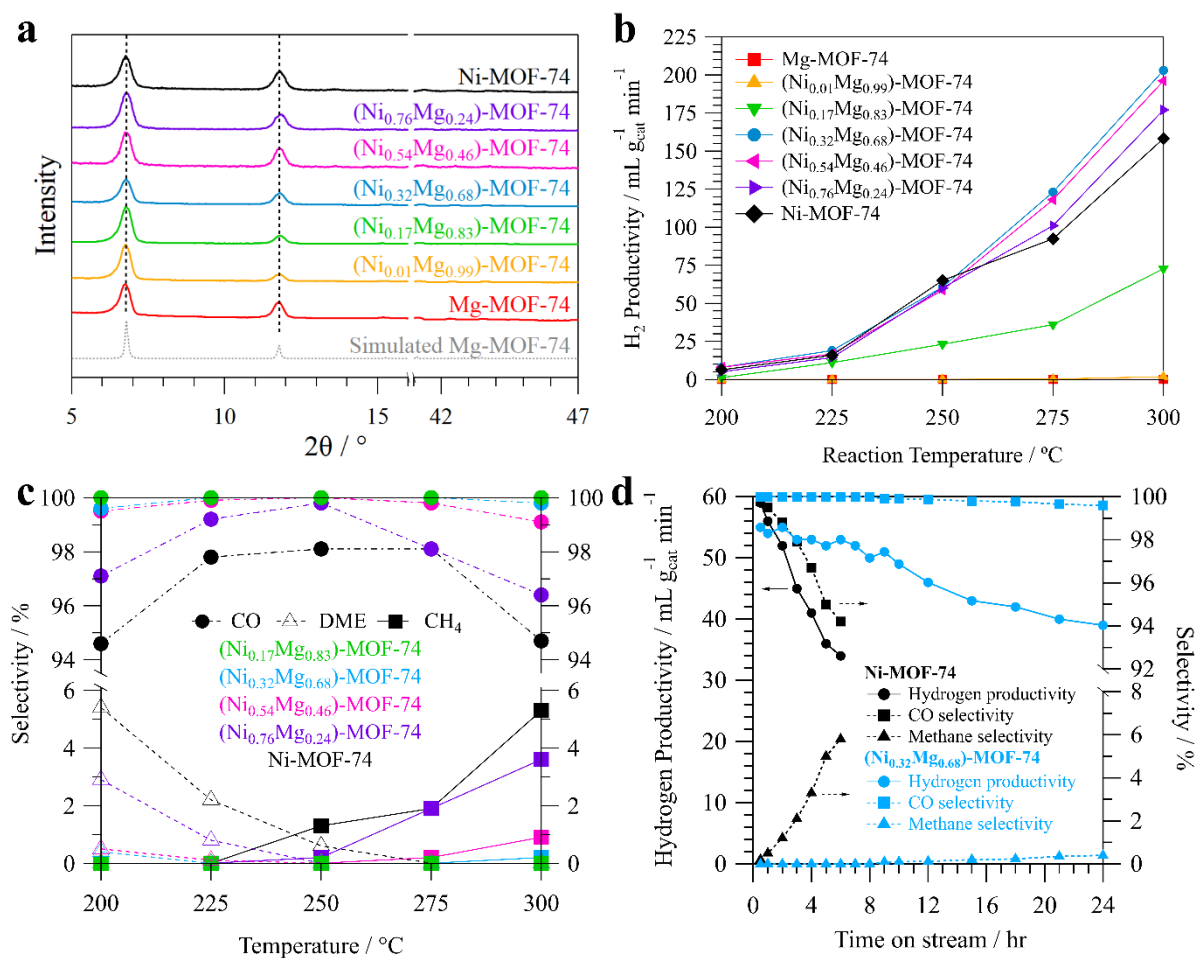


**Figure 4.** (a) Normalized XRD patterns of the ‘as synthesized’  $(\text{Ni},\text{Mg}_{1-x})\text{-MOF-74}$  catalyst series, compared against a simulated Mg-MOF-74 reference (CSD-VOGTIV).<sup>1</sup> Catalytic performance of the synthesized  $(\text{Ni},\text{Mg}_{1-x})\text{-MOF-74}$  towards methanol dehydrogenation: (b) hydrogen productivity normalized to the total mass of catalyst, (c) product selectivity towards CO (solid circles), DME (open triangles) and  $\text{CH}_4$  (solid squares), and (d) stability of methanol dehydrogenation at 250  $^\circ\text{C}$  for Ni-MOF-74 and  $(\text{Ni}_{0.32}\text{Mg}_{0.68})\text{-MOF-74}$ . Reaction conditions: 0.1  $\text{mL min}^{-1}$  methanol, 35 sccm  $\text{N}_2$ , 100 mg catalyst, 1 atm.

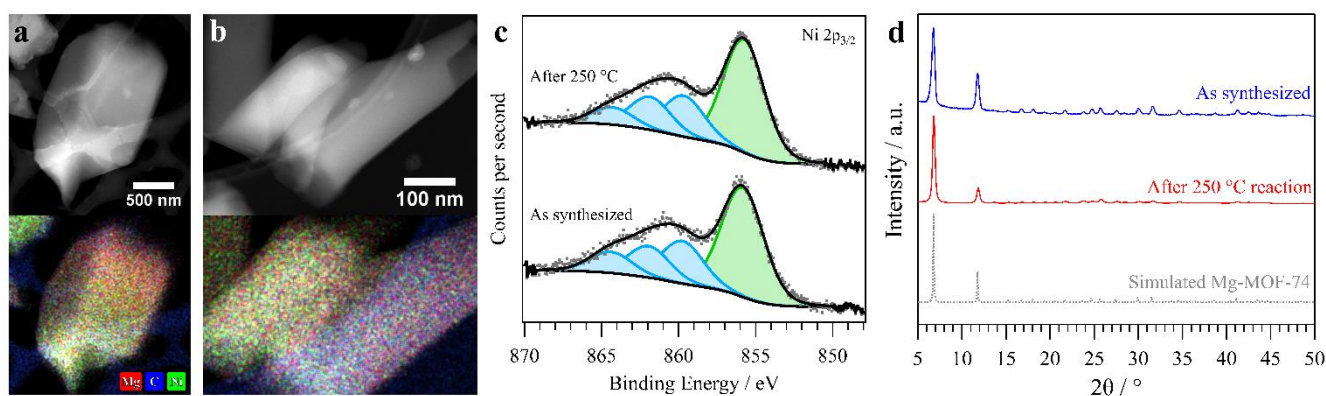


**Figure 5.** Characterization of  $(\text{Ni}_{0.32}\text{Mg}_{0.68})\text{-MOF-74}$  before and after performing methanol dehydrogenation for 1 hour at 250  $^\circ\text{C}$  and 1 atm. Dark field TEM images and TEM-EDS maps of the catalyst (a) before testing and (b) after testing, showing magnesium (red), carbon (blue), and nickel (green). (c) Ni  $2p_{3/2}$  XPS spectra of the catalyst before and after testing. Experimental data (grey points) fit with a  $\text{Ni}^{2+}$  peak (green) and several satellite peaks (blue) to create the envelope shown (black line). (d) XRD patterns of the catalyst before and after testing, compared to a simulated Mg-MOF-74 reference (CSD-VOGTIV).<sup>1</sup>

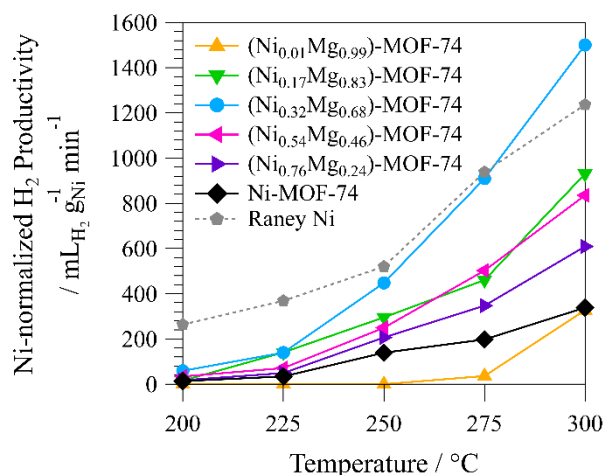


**Figure 6.** Hydrogen productivity of the catalyst series for methanol dehydrogenation, normalized to the nickel content as determined by SEM-EDS. Commercial Raney Ni, dried under vacuum and handled under  $N_2$ , used as a nickel standard and normalized to its total mass. Reaction conditions:  $0.1 \text{ mL min}^{-1}$  methanol, 35 sccm  $N_2$ , 100 mg MOF catalyst (45 mg Raney Ni), 1 atm.

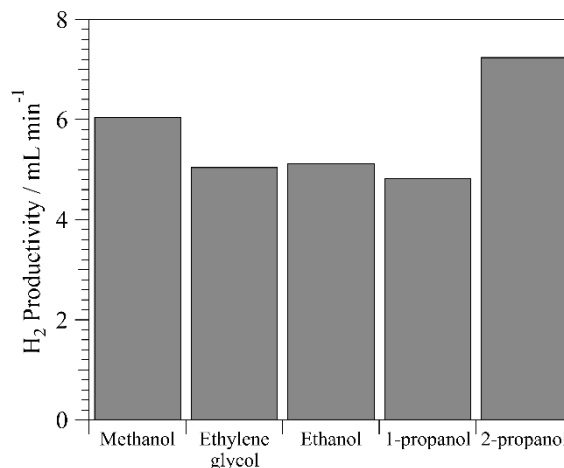


**Figure 7.** Hydrogen productivity, averaged over 1.5 hours, from alcohol-based hydrogen carriers using  $(Ni_{0.32}Mg_{0.68})$ -MOF-74 catalyst. Reaction conditions:  $0.1 \text{ mL min}^{-1}$  liquid feed ( $0.05 \text{ mL min}^{-1}$  for ethylene glycol), 100 mg catalyst, 35 sccm  $N_2$ , 1 atm,  $250 \text{ }^\circ\text{C}$ .

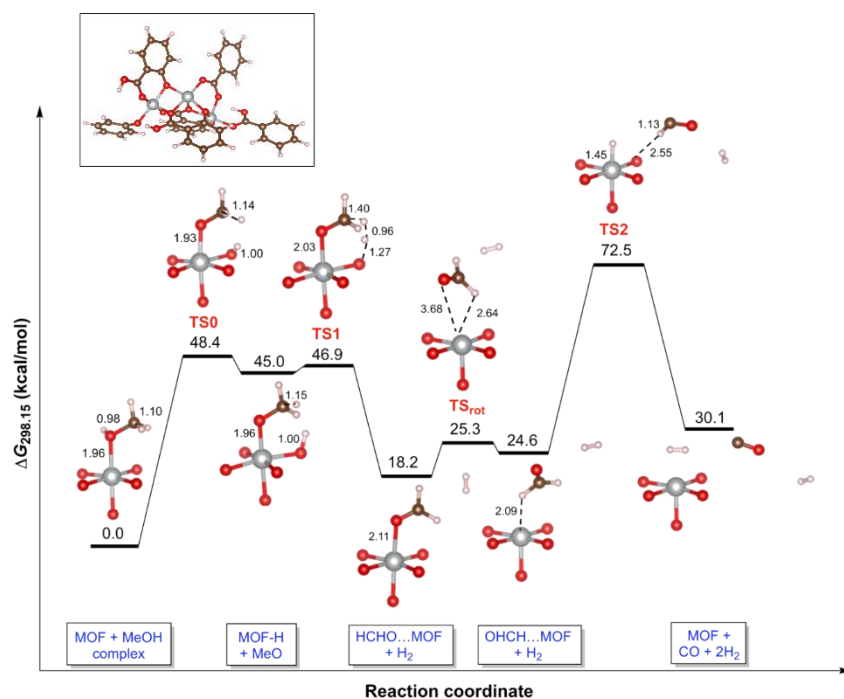


**Figure 8.** Gibbs free energy profile ( $\Delta G_{298.15}$  in kcal/mol) of the conversion of methanol into carbon monoxide and hydrogen on Ni-MOF-74 calculated using PBE/def2-TZVP. The  $\Delta G_{298.15}$  values of each species are relative to the MOF + MeOH complex. For visual clarity, only the first coordination sphere of Ni-MOF-74 and key bond distances (in Å) are shown for each structure of the catalytic cycle. As shown in the full cluster model (inset), the linker molecules provide the O atoms shown. TS0 (not given in Table 1) is the first transition structure of the catalytic cycle that involves the transfer of a H atom from methanol to the O atom of the linker. TS<sub>rot</sub> (not given in Table 1) is the transition structure for the rotation of HCHO. For some of the structures more than one conformer were located, which differ in energy by a few kcal/mol. [Color coded such that Ni = gray, O = red, C = brown, and H = white.] Transition structures for other M-MOF-74 structures can be found in Figure S12.

**Table 1.** Barrier heights ( $\Delta G^\ddagger$ , kcal/mol)<sup>a</sup> and reaction energies ( $\Delta G$ , kcal/mol)<sup>b</sup> of (1) the dehydrogenation of methanol to formaldehyde and (2) the dehydrogenation of formaldehyde to carbon monoxide for the reaction catalyzed by each M-MOF-74 and referenced against the uncatalyzed reaction. Lower barrier heights are observed when the reaction at the OMS is assisted by the linker, as shown in Figure 8. Gibbs free energies calculated by PBE/def2-TZVP using the cluster model.

Metal in M-MOF-74	Catalysis at unassisted OMS				Catalysis at OMS assisted by linker			
	$\Delta G^\ddagger_1$	$\Delta G_1$	$\Delta G^\ddagger_2$	$\Delta G_2$	$\Delta G^\ddagger_1$	$\Delta G_1$	$\Delta G^\ddagger_2$	$\Delta G_2$
Cu	75.3	18.9	73.1	2.7	11.5	-20.7	63.1	4.2
Co	71.8	18.1	78.9	6.1	11.2	-17.9	48.3	5.3
Mg	68.5	22.2	80.0	8.4	1.3	-29.0	61.4	3.9
Mn	76.7	20.6	78.6	7.5	5.0	-22.7	49.9	3.3
Ni	77.2	20.6	81.4	10.3	1.9	-26.8	47.3	4.9
Zn	76.9	18.3	78.3	5.0	3.6	-24.7	57.0	4.2
Uncatalyzed	80	13	74	-1	-	-	-	-

<sup>a</sup>The barrier heights are calculated with respect to the immediate intermediate preceding the transition structure.

<sup>b</sup>Reactant adsorption and product desorption are not considered in the reaction energies. The reaction energies are calculated as the difference in energies between the product complex and the reactant complex.